Solar Energy 279 (2024) 112811

Contents lists available at ScienceDirect

Solar Energy

journal homepage: www.elsevier.com/locate/solener

In-situ UNet-based heliostat beam characterization method for precise flux calculation using the camera-target method

Mathias Kuhl [a,b,*], Max Pargmann [a], Mehdi Cherti [b], Jenia Jitsev [b], Daniel Maldonado Quinto [a], Robert Pitz-Paal [a,c]

[a] DLR, Institute of Solar Research, Linder Höhe, Köln, 51147, Germany
[b] FZJ, Jülich Supercomputing Centre, Wilhelm-Johnen-Straße, Jülich, 52428, Germany
[c] RWTH Aachen University, Chair of Solar Technology, Linder Höhe, Köln, 51147, Germany

ARTICLE INFO

Keywords:
Flux measurement
Solar power tower
Camera-target method
Beam characterization
Digital image analysis

ABSTRACT

Concentrated Solar Power (CSP) utilizing solar tower power plants exhibits significant potential for dispatchable sustainable power generation and fuel production, by concentrating up to hundred thousand focal spots of individual mirrors onto one surface. The irradiance on the receiver is a critical parameter for power plant operators, not only to prevent component-damaging temperature peaks and gradients but also to optimize the distribution of heliostat's focal spots. Therefore, recent approaches aim to exploit images of isolated focal spots on a Lambertian target, taken on a day-to-day basis in most commercial power plants, to achieve more accurate flux predictions. State-of-the-art methods for flux measurements require additional equipment and are mostly time-intensive. This study introduces a novel methodology to derive single heliostat irradiance profiles using simple digital camera images, employing an image-to-image neural network. The model we propose is capable of generating accurate, high-resolution flux distributions from single images. It uniquely accounts for the target surface's irregularities and reflectivity as well as background irradiation, factors critical for precise measurements of individual focal spots. By incorporating these factors, our methodology offers a new scaling approach for the measured flux density based on a calculated total flux, obviating the need for additional equipment such as flux gauges or moving bars. This enables effortless integration into the daily calibration routine in-situ using the camera-target method. This seamless integration not only supports existing flux prediction methodologies but also paves the way for future enhancements by potentially improving the accuracy of overall flux prediction.

1. Introduction

Concentrated Solar Power (CSP) represents an innovative and environmentally friendly technology with significant potential for dispatchable power generation through thermal energy storage and in solar fuel production [1,2]. Solar tower plants employ an array of heliostats, adjustable mirrors, to track the sun and focus its rays onto a central receiver or reactor, leveraging this concentrated sunlight for diverse applications.

A thorough understanding of solar irradiance on the receiver is crucial for plant operators for several reasons. It helps in prolonging the lifespan of the plant by preventing damage to the receiver from abrupt heat spikes and temperature variations. Additionally, insights into solar irradiance enable the strategic realignment of heliostats [3], yielding more consistent and efficient energy production throughout the year. Recent studies indicate that improved aimpoint strategies could significantly boost annual revenue, exemplified by projections of up to a 39% increase for facilities like Gemasolar in Almeria [4]. Given that total irradiance is a superposition of individual contributions from each heliostat, each with its unique focal spot, there is a growing research focus on utilizing target images for precise predictions of single heliostat focal spots [5–8]. However, current camera-based flux calculation methods are hampered by limitations. Most of them are to time-intensive or need additional measurement equipment.

Addressing these challenges, our study introduces an innovative in-situ method to determine the absolute irradiance profile of individual heliostats using straightforward digital camera images, complemented by Direct Normal Irradiance (DNI) measurements. Central to our approach is the application of an image-to-image neural network, specifically a UNet architecture. The UNet is designed to learn the mapping between two types of images; in our case, it maps target images to flux

* Corresponding author at: DLR, Institute of Solar Research, Linder Höhe, Köln, 51147, Germany.
E-mail address: mathias.kuhl@dlr.de (M. Kuhl).

https://doi.org/10.1016/j.solener.2024.112811
Received 3 February 2024; Received in revised form 7 June 2024; Accepted 25 July 2024
Available online 9 August 2024

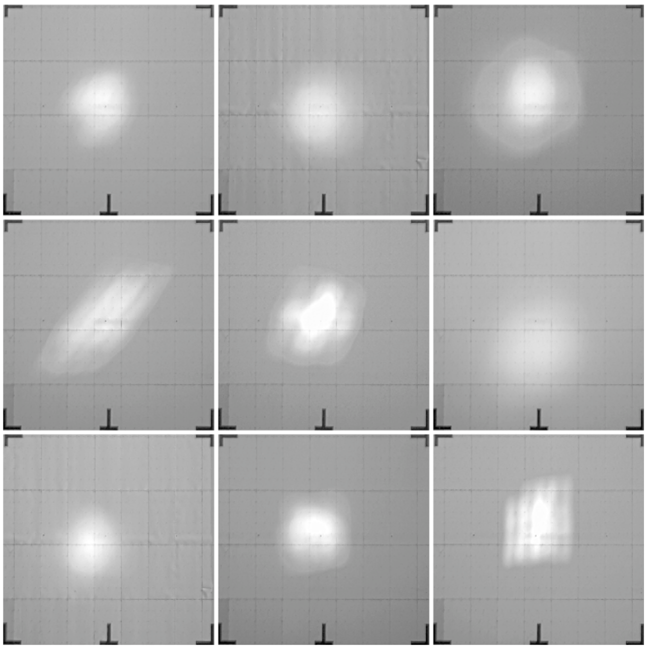

Fig. 1. Sample target images from the STJ depicting focal spots of various heliostats under different sun positions. These images illustrate the variations in background radiation, as well as the diversity in position and intensity of each focal spot.

distribution. During training, the model learns to filter out background irradiation from single target images and account for the spatial target reflectivity of the surface. We use simulated data to train the model leveraging images of the target without a focal spot, to reproduce different background irradiation conditions, and superpose a simulated focal spot from a raytracer. This model excels in calculating smooth, high-resolution flux distributions, which are scaled by the calculated total flux of the focal spot.

2. State of the art

2.1. The camera-target calibration procedure

Our method leverages images, obtained by the camera-target procedure, initially proposed by Stone [9]. This method involves relocating the focal spot of a single heliostat to a Lambertian target positioned beneath the receiver. A camera, placed within the heliostat field, captures the radiation reflected off the target surface. Fig. 1 shows examples of such target images obtained at the Solar Tower in Jülich (STJ) [10]. These images are preprocessed to correct any distortions; this involves using marker detection algorithms to identify marker positions at the target's edges, which are then used to crop and rectify the raw image.

During power plant operation these images are primarily analyzed to determine the centroid of the focal spot, aiding in the calibration of the heliostat's alignment model. The camera-target method is widely recognized as one of the most established techniques in power plant operations for heliostat calibration [11]. Various researchers, including Smith and Ho [12], Guangyu and Zhongkun [13], and Pargmann et al. [14], have utilized this method to calibrate different heliostat models and predict alignment errors.

Calculating flux profiles from these images poses significant challenges. The images typically consist of the target's background irradiation superimposed with the focal spot. Background illumination can significantly influence the camera pixel intensity for single heliostat measurements, making its inclusion in analysis crucial. The variability in both the position and intensity of the focal spots, coupled with changes in background irradiation, complicates the task for conventional image processing algorithms. These algorithms struggle to differentiate between background radiation and radiation reflected from the heliostat, which is critical for determining flux density distributions of single heliostat focal spots in an automated manner. Common approaches, such as subtracting background irradiation by capturing a reference image of the empty target immediately prior to measurement, have proven to be only partially effective. This limitation is often attributed to irradiation fluctuations between the two captures and the extended calibration time required for acquiring multiple images.

Furthermore, the reflectivity of the target surface is a pivotal factor in accurately determining flux density distributions from target images. Over time, the target area may degrade, affecting its reflectivity. This degradation can lead to spatial variations in reflectivity, adding another layer of complexity to the image processing task.

2.2. Predicting heliostat focal spots

Predicting the focal spots of heliostats, while accounting for canting and mirror errors, is a complex task with various existing approaches. As summarized by Garcia et al. [15], the most prevalent methods are convolution techniques and Monte Carlo Raytracing. Convolution methods, demonstrated by Schwarzbözl et al. [16], involve the mathematical superposition and convolution of error cones from individual heliostats. On the other hand, Monte Carlo Raytracer techniques, used by Leary and Hankins [17], Wendelin [18], Roccia et al. [19] or Belhomme et al. [20], either involve simplifications or require complex and costly surface measurements, such as deflectometric measurements [21] or photogrammetry [22], which are unreliable or expensive, limiting their practicality for large-scale heliostat applications.

In response to these limitations, more recent approaches by Rodríguez-Sánchez et al. [6] and Pargmann et al. [8] have been proposed. These methods leverage target images to derive more accurate flux predictions for individual heliostats. A significant advantage of these methods is their ability to utilize images acquired during routine calibration processes.

2.3. Flux density measurement

A variety of direct and indirect methods exist for measuring flux distributions, as summarized by Röger et al. [23]. Many of these methods are designed to measure the superposed flux density distributions from the entire heliostat field, typically at the aperture plane of the receiver or reactor.

Direct methods, such as those involving moving bars [24] or a moving focus [25], are not ideal for our approach. The requirement to move the target or focus renders the process too time-intensive for measuring individual focal spots.

On the other hand, indirect methods like the camera-target method calculate the spatial distribution of energy flux using diffusely reflected light from a Lambertian target illuminated by one or more heliostats. This approach necessitates an assessment of target surface irregularities and spatial variations in reflectivity to accurately scale the flux. Additionally, flux gauges are often required to obtain an absolute flux value for scaling the distribution, as noted by Rodríguez-Sánchez et al. [6].

Our study aims to address these limitations by introducing a novel methodology that leverages image-to-image neural networks for precise, efficient, and cost-effective flux prediction. By capitalizing on the advancements in digital image processing and neural network capabilities, our approach proposes to enhance the accuracy of flux density measurements while simplifying the acquisition process of the flux density profiles.

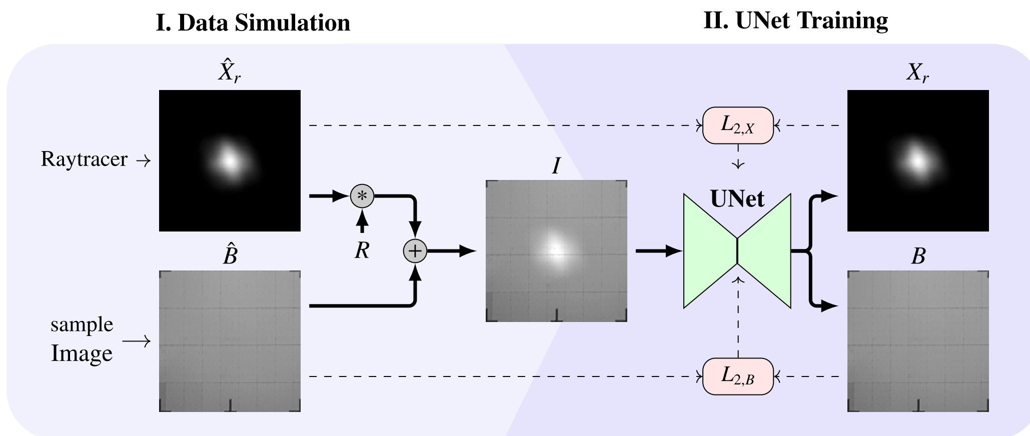

Fig. 2. A raytracer is used to generate realistic focal spots $\hat{X}_R$, which are multiplied with the spatial reflectivity R of the target and superposed with a randomly sampled image of the empty target $\hat{B}$. The UNet learns to split the simulated image I back into its components X_R and B. Pixel-wise L2-Losses $L_{2,i}$ are calculated between the UNet's outputs and the desired groundtruths and serve the UNet as a training loss.

3. Method

The aim of our methodology is to derive highly resolved flux distributions, denoted as X, in W m^{-2} from the observed image I. We recognize that the observed image I is a superposition of ambient illumination I_A and incident heliostat flux X_r, both reflected from the target surface, mathematically represented as follows:

$$I = R \cdot (X_r + I_A) = R \cdot X_r + B \tag{1}$$

$$X = c \cdot X_r \tag{2}$$

In these equations, R signifies the spatial target reflectivity. The background image $B = I_A \cdot R$ is the reflected background illumination I_A observed in image I. X_r is a relative flux distribution, and c is the scaling factor. The relative flux X_r within our images is proportionally related to the desired absolute flux X, modulated by the scaling factor c. Given the absence of detailed information about the camera's settings, such as shutter speed, ISO settings, or the color spectrum characteristics of the flux, directly converting pixel intensity to flux intensity in W m^{-2} proves to be a challenge. To bypass this, we utilize a simplified heliostat model to estimate the total energy flux $\dot{Q}_{spot}$ in the observed focal spot. This estimation is then used to calculate the scaling factor c, as shown in the equation:

$$c = \dot{Q}_{spot} / \dot{Q}_{image} \tag{3}$$

Here, $\dot{Q}_{image}$ represents the total energy of the computed relative flux X_R, which can be calculated under the assumption that its pixel intensities reflect values in W m^{-2}.

3.1. Determination of the relative flux distribution

Accurate determination of relative flux distributions, denoted as X_r, from images is essential for proper scaling in our method. As detailed in Eq. (1), each observed image is a composite of background illumination and reflected flux. When measuring single heliostat focal spots, which typically have relatively small concentration factors, the background illumination significantly contributes to the pixel intensity. Ignoring this factor could lead to an undesirable offset in X_r and, consequently, inaccurate absolute flux values X. The variability in the position and intensity of the focal spots, along with fluctuating background irradiation, presents a challenge for standard image processing algorithms to effectively differentiate between background radiation and heliostat-reflected radiation, complicating the automated determination of flux density distribution. Approaches, such as subtracting background irradiation using a reference image of the empty target taken immediately before the measurement, have limited success. This limitation is often due to instabilities arising from irradiation changes between successive measurements and the increased calibration time required for capturing multiple images.

To overcome these challenges, we introduce an image-to-image neural network designed to distinguish between radiation from the flux spot and background radiation. This network is adept at detecting the entire intensity range in the image related to the focal spot, including areas with weak illumination. This task is akin to image segmentation in computer vision, where models learn to map an input image to a corresponding pixel-wise segmentation map. Such maps assign semantic labels to each pixel, facilitating detailed object and area recognition. The UNet architecture, particularly the UNet3+ variant proposed by Huang et al. [26], has demonstrated excellent performance in image segmentation across various fields. The goal of our network is to separate the focal spot from the background while maintaining the irradiance intensity independent of background illumination. In this setup, the camera image I serves as the input to the model U, with the target outputs being the relative flux density distribution X_r and the background image B:

$$X_r, B = \mathbf{U}(I) \tag{4}$$

While the background image B is not our primary focus, it is useful for validating the accuracy of the model's background estimation. Furthermore, incorporating auxiliary tasks alongside the main objective is expected to enhance overall performance [27]. Flux calculation, the main objective, necessitates background subtraction as an essential step. Actively engaging the network to determine the background B as an auxiliary task promises to enhance the accuracy of the flux calculation. To effectively train the UNet, it is necessary to have sets of corresponding values for X_r, B, and I. During the training stage those properties are unknown for observed images I; therefore, we resort to generating simulated target images with predefined flux X_r and background B. This simulation process ensures that we have control over the properties of the images used for training our model U. Once trained with these simulated images, which mimic realistic conditions, our model is then well-equipped to be applied to actual field images.

3.1.1. Background irradiation

To acquire samples of B, we capture images of an empty target devoid of any focal spot. These images possess characteristics similar to B in the composite image I. Throughout the year, we collected over 1000 such images of the empty target under various irradiation conditions to capture a broad range of irradiation scenarios. Given that the images B are captured using the same camera settings as the images I, they can be directly utilized without the need for additional scaling. During the data simulation process, background images B are randomly sampled from the entire dataset and can be used multiple times combined with different fluxes X_r to generate different artificial images I.

3.1.2. Spatial reflectivity

For calculating reflectivity R, we assume the target surface exhibits Lambertian properties, diffusely and uniformly reflecting light across all wavelengths. In these empty target images denoted as B, we consider only the reflected ambient light $B = R \cdot I_A$, where I_A symbolizes the ambient irradiation. Although individual measurements of B may show spatial variations in I_A, averaging a large number of B measurements should yield a consistent mean ambient illumination I_A over the entire target. Thus, we calculate relative reflectivity R using the equation:

$$R = \overline{B}/max(\overline{B}) \tag{5}$$

Here, $\overline{B}$ denotes the pixelwise mean value across all images B, normalized by the maximum pixel value $\max(\overline{B})$. This normalization yields a relative reflectivity R that ranges between 0 and 1, corresponding proportionately to the actual reflectivities. Since our objective is to work with relative flux values X_r and scale it correctly afterwards, a relative reflectivity is sufficient. In our simulation process, by incorporating reflectivity, we allow the network to directly predict the incident flux, taking into account target reflectivity and irregularities, rather than just the reflected flux captured in the image. We assume that the reflectivity R is constant for all images.

3.1.3. Incident heliostat flux

The final component in Eq. (1) involves simulating the flux distributions X_r. We utilize a raytracer with surface measurements from a deflectrometry to create highly realistic representations of focal spot shapes. While the actual intensity or absolute flux values are not critical for this simulation, we adjust the intensity of the reflected flux $R \cdot X_r$ to align with the intensities observed in our actual target images I. We did this by scaling the raytracing values also to image pixel values between 0 and 1. To more accurately simulate realistic pixel intensity ranges for X_r, we analyzed the pixel intensities of background images B and images with focal spots I. This comparison revealed that the heliostat flux contributes between 60% and 90% of the pixel intensity at the center of the focal spot. Consequently, we adjust the scaling of X_r so that the maximum value of the reflected heliostat flux, $X_r \cdot R$, falls within the 0.6 to 0.9 range before it is combined with B. For each simulated image I, the specific scaling factor is randomly selected within this interval during the data simulation process. Fig. 2 illustrates the complete simulation procedure. This approach allows us to generate an unlimited number of data pairs for the effective training of our UNet model. Appendix provides several examples of the generated data pairs.

3.1.4. UNet

To solve our task of we employ the UNet3+ architecture introduced in [26]. We adapted the input and output size of the network to align with our specific problem. The input dimensions of the network are set to $1 \times 256 \times 256$, corresponding to the grayscale target input image I with resolution 256×256. The output dimensions are configured as $2 \times 256 \times 256$, representing the flux density X_r and background B, with each output channel dedicated to one of these components and maintaining the same resolution as the input images I. The Encoder-Decoder architecture of the UNet comprises 5 levels, each consisting of downscaling and upscaling blocks that regulate the data flow through the network. In the downscaling blocks, the spatial dimensions of the image are progressively reduced, enabling the network to capture essential features at multiple resolutions. This encoding process transforms the input image into a compact and informative representation. Conversely, the upscaling blocks incrementally restore the spatial dimensions of the encoded representation back to the original image size. This ensures that the final output is both detailed and accurate, preserving the spatial integrity and context of the original input. At each level, the number of feature channels, denoted as f_i, increases, with values set in the range $[32, 64, 128, 256, 512]$.

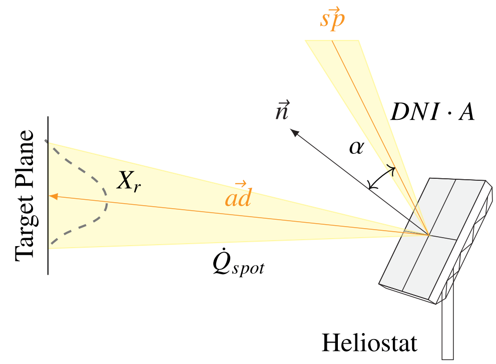

Fig. 3. Schematic drawing of the Heliostat Model used for calculating the total reflected energy flux $\dot{Q}_{spot}$. The model illustrates how the incoming solar flux $\dot{Q}_{inc} = DNI \cdot A_H$, arriving from direction $\vec{sp}$, is reflected towards direction $\vec{ad}$ at the heliostats mirror surface. This process results in a reflected beam characterized by the total energy flux $\dot{Q}_{spot}$ and a spatial flux distribution X_r.

During the training phase, we utilize the simulated data pairs described earlier. Contrary to typical segmentation tasks that aim to generate binary segmentation masks (values 0 or 1), our goal with the UNet is to model continuous intensity distributions with values ranging between 0 and 1. Therefore, to better train our model to output these distributions, we replace the commonly used pixel-wise cross-entropy loss with a pixel-wise L2-loss. This loss function computes the mean squared error (MSE) between the network's predicted outputs X_r and B and their respective ground truth values $\hat{X}_r$ and $\hat{B}$ for each pixel. These ground truths are based on the known properties of our simulated target images. The total training loss $\mathcal{L}$ is formulated as:

$$\mathcal{L} = L_{2,X} + L_{2,B} \tag{6}$$

$$L_{2,X} = \frac{1}{N}\sum_{i}^{N}(X_i - \hat{X}_i)^2 \tag{7}$$

$$L_{2,B} = \frac{1}{N}\sum_{i}^{N}(B_i - \hat{B}_i)^2 \tag{8}$$

In these equations, $L_{2,X}$ and $L_{2,B}$ represent the pixel-wise L2-Losses for X_r and B respectively, and N is the total number of images in each training batch. The details of this training procedure are further illustrated in Fig. 2.

3.2. Camera specifications and image processing

For our purposes, we use a CMOS RGB camera deployed in the heliostat field. The color channels are translated to grayscale through a linear conversion, where the red and blue channels are weighted equally and the green channel is weighted twice as much. This weighting is based on the sensor density in the CMOS camera for each respective color. Within our procedure, any linear grayscale conversion is suitable.

Our method involves the model learning to remove the background, including dark current, from numerous samples of images devoid of focal spots. This allows us to assume that the remaining signal is solely due to the heliostat flux and is therefore proportional to it. Consequently, the camera error can be estimated based on the linearity of the sensors, which in our case is below 1%. Overall, the method is applicable to any camera type, with the error being dependent solely on the linearity of the sensors.

3.3. Translation of relative to absolute flux distribution

Up to this point, we have obtained a precise relative flux X_r that is proportional to the desired absolute flux X. For accurately translating these relative flux values X_r to absolute flux values X in $\mathrm{W\,m^{-2}}$, we adopt a methodology to scale the total flux of the focal spot, as detailed in Eq. (3). We use an approach to calculate the total energy flux of an heliostat similar to common to state of the art approaches to calculate heliostat field efficiencies [28,29]. We extend its use by scaling a measured relative intensity distribution with the calculated total energy to derive a spatially resolved energy distribution, facilitating a broader range of applications.

In our model, the heliostat responsible for reflecting sunlight to create the observed focal spot is depicted in Fig. 3. Our primary target is to calculate the incident total flux $\dot{Q}_{spot}$ of the focal spot on the target. This is achieved by employing the Direct Normal Irradiance (DNI) and the effective mirror area A_{eff}, combined with the heliostat mirror reflectivity r:

$$\dot{Q}_{spot} = r \cdot DNI \cdot A_{eff} \tag{9}$$

The effective mirror area A_{eff} is determined by calculating the angle of incidence α of the sun's rays onto the heliostat surface. This incident angle α is derived by considering both the sun's position $\vec{sp}$ and the heliostat's aim direction $\vec{ad}$. The sun's position $\vec{sp}$ is based on the time of measurement, while the aim direction $\vec{ad}$ is the vector from the heliostat to the center of the observed focal spot. Assuming the mirror's normal $\vec{n}$ aligns with the reflection, α is calculated as half the angle between the incident and reflected directions:

$$\alpha = \frac{1}{2} \cdot \angle(\vec{sp}, \vec{ad}) \tag{10}$$

$$A_{eff} = cos(\alpha) \cdot A_H \tag{11}$$

Here, A_H is the mirror area projected in the direction of incidence. For the effective mirror area canting of the mirror facets could be taken into account. At the STJ the heliostats are barely canted, therefore this effect is negligible. DNI, crucial for every flux prediction method, is routinely measured at CSP plants, making it readily available for our method. Additionally, the reflectivity r of representative heliostats in the field is monitored biweekly at the STJ to assess their current condition.

To ascertain the energy $\dot{Q}_{image}$ of the normalized distribution X_R, we set that pixel intensities in the image represent flux per unit area $\dot{q}$ in $\mathrm{W\,m^{-2}}$. The total flux in the image $\dot{Q}_{image}$ and the scaling factor c are calculated to match the total flux $\dot{Q}_{spot}$:

$$\dot{Q}_{image} = A_T \cdot \dot{q}_{image,avg} \tag{12}$$

$$c = \frac{\dot{Q}_{spot}}{\dot{Q}_{image}} = \frac{r \cdot cos(\alpha) \cdot DNI \cdot A_H}{A_T \cdot \dot{q}_{image,avg}} \tag{13}$$

Here, A_T denotes the area of the target plane and $\dot{q}_{image,avg}$ represents the average pixel value of X_r. Our simplified heliostat model requires certain conditions to be met for accuracy. It is essential that there is no shading or blocking of the flux by clouds or other heliostats. The entire focal spot must be visible on the target without any spillage flux; otherwise, we cannot correctly calculate the total energy of the observed flux. Fulfilling these conditions ensures the accuracy of our model.

4. Results

Fig. 4 showcases the results obtained using our methodology. The UNet, trained on simulated data, was applied to actual target images from the Solar Tower Jülich (STJ). In the first row of the figure, nine sample target images I are displayed under varying conditions. Below, we observe the calculated relative flux distributions X_r and the predicted background radiations B, both derived using the UNet model. The determined X_r distributions are notably smooth and effectively capture all nuances in the focal spots, including regions of weak illumination or those with slight variances in brightness. Likewise, the predicted background B accurately reflects various conditions of background intensity and the superimposed focal spot.

To quantify the accuracy with which the flux X_r is reconstructed from image I, we introduce a pixel deviation measure. This metric assesses the relative mean pixel deviation between X_r and its ground truth $\hat{X}_r$:

$$L_{pix,X} = \frac{\sum_i |X_{r,i} - \hat{X}_{r,i}|}{\sum_i |\hat{X}_{r,i}|} \tag{14}$$

Here, i represents pixel indices. This deviation was calculated during the training of our UNet on a test set of images not used during training, revealing a deviation of 1.5%. This figure indicates the level of accuracy achieved in the relative flux distribution X_r.

In the final row of Fig. 4, we display the scaled absolute flux densities in $\mathrm{kW\,m^{-2}}$, as calculated by our method. To assess the accuracy of these absolute flux values X, we need to scrutinize each component involved in Eq. (13). It is reasonable to assume that geometric parameters such as surface areas A_T, A_H, and the incident angle α are accurate. Reflectivity measurements at the STJ, conducted biweekly, show that reflectivity deviations between different heliostats typically stay below 1%, with similar margins for time-dependent variations between two measurements. Notable events that significantly impact reflectivity, like storms or rainfall, are monitored and accounted for with subsequent measurements. As a result of our analysis, we have determined the uncertainty associated with the measured reflectivities, denoted by r, to not exceed an error margin of $err_r = \pm 2\%$. Furthermore, the error margin for Direct Normal Irradiance (DNI) measurements has been ascertained to be below $err_{DNI} = 1\%$. The inaccuracies stemming from camera errors due to the non-linearity of the sensors are evaluated to be under $err_{Cam} = 1\%$. In terms of the UNet model's performance, the accuracy is quantified by the relative flux deviation, with $err_{UNet} = 1.5\%$. Furthermore, potential errors in the total energy calculation may arise from spillage losses err_{spill} and shading or blocking losses err_{SB}. However, based on the assumptions outlined in Section 3.3, these errors are considered negligible in our analysis.

We implement the error propagation method to quantify the cumulative uncertainty in our methodology. The total error, denoted as err_{total}, is calculated using the following formula:

$$err_{total} = \sqrt{err_r^2 + err_{DNI}^2 + err_{Cam}^2 + err_{UNet}^2 + err_{spill}^2 + err_{SB}^2}$$

Through the application of this method, we have determined the overall error of our methodology to be approximately 4.5%.

5. Discussion

The implementation of a UNet-based image-to-image neural network for heliostat beam characterization in the camera-target method represents a notable advancement in the field. This study demonstrates the method's proficiency in accurately predicting relative flux distributions from single digital camera images. It addresses crucial limitations of existing camera-target methodologies by factoring in background irradiation, target irregularities, and surface reflectivity. The utilization of the UNet architecture for accurate flux distribution predictions is particularly noteworthy, as it can be seeminglessly included into the heliostat calibration process, as it works on single images. This approach is poised to enhance any method that relies on such images as no other known method robustly and fully automates compensation for background illumination and target anomalies. The flux data obtained through our approach are readily applicable to superposition methods, like the one outlined by Rodríguez-Sánchez et al. [6], enabling the direct calculation of the cumulative flux density from all heliostats. Additionally, these data can facilitate the extraction of surface information for individual heliostats, enhancing raytracing simulations as detailed in Pargmann et al. [8].

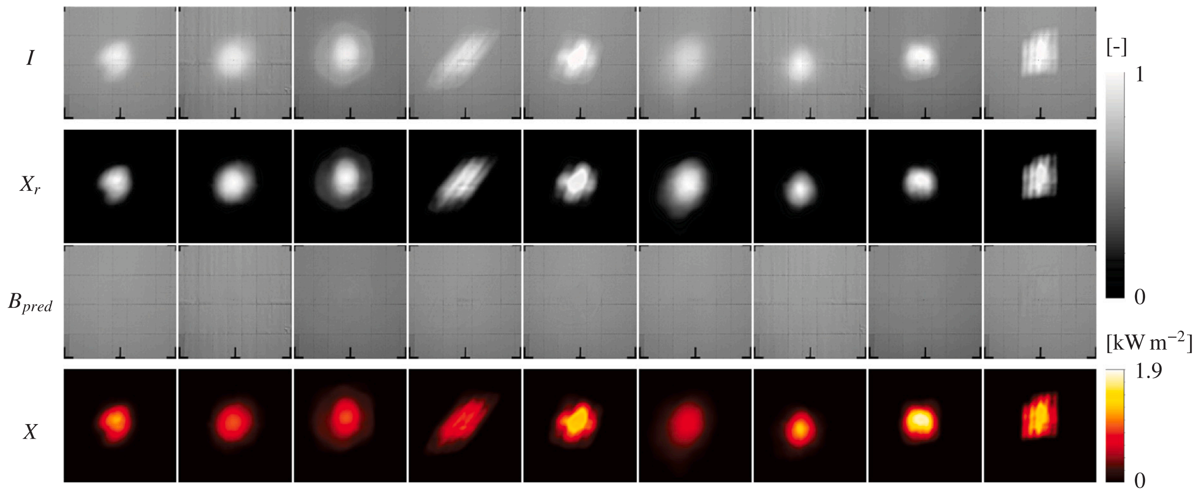

Fig. 4. Application of Our Method to nine Sample Images I: The rows labeled X_r and B display the UNet's predictions for relative flux and background irradiation, respectively. The final row, labeled X, illustrates the calculated absolute flux values, as determined using our proposed methodology.

Comparing our scaling approach with state-of-the-art methods like those suggested by Rodríguez-Sánchez et al. [6], which employ flux gauges, we observe distinct differences in the uncertainty profiles. Both camera inaccuracies and DNI measurements affect all flux measurement systems uniformly, depending on the chosen equipment and methodology. In contrast, other methods primarily grapple with the uncertainty inherent in flux gauge measurements, typically around $\pm 3\%$ [23]. Our method, on the other hand, primarily contends with the uncertainty in heliostat reflectivity r, estimated at around $\pm 2\%$. Thus, it potentially offers comparable, if not superior, accuracy without the necessity for additional flux gauges, relying instead on frequent reflectivity measurements commonly conducted at power plants. Nevertheless, the calculation of the relative flux via the UNet operates independently of the scaling approach. Retaining the advantages of the UNet, the total energy scaling could potentially be substituted with a radiometric point measurement on the target plane. Additionally, employing both, radiometric measurement and total energy calculation, might be beneficial. This combination could allow for more accurate radiometer calibration using total energy calculations or alternatively, enable the determination of heliostat mirror reflectivities from measured intensities of the focal spots.

Despite the strengths of our methodology, it is important to acknowledge its dependencies and limitations. Our approach assumes the absence of shading or blocking and necessitates that the entire focal spot is visible on the target without any flux spillage. These conditions, if unmet, could limit the method's applicability in certain CSP plant configurations, necessitating adjustments to the heliostat model. Also, in our simulations, we utilized a raytracer paired with surface measurements from deflectometry. While such resources may not be universally available at every power plant, the raytracer could be substituted with simpler models or assumptions about the characteristics of the focal spots.

6. Conclusion and outlook

This study introduces an innovative UNet-based methodology for heliostat beam characterization within the camera-target method framework in Concentrated Solar Power (CSP) plants. By utilizing a neural network to process single digital camera images, our method markedly enhances the accuracy of flux distribution calculations. Crucial advancements include accounting for background irradiation, irregularities on the target surface, and reflectivity. These enhancements address significant limitations of conventional camera-target methods. The incorporation of UNet architecture into the heliostat calibration process marks a considerable advancement, ensuring smooth integration into existing operational workflows and promising to significantly improve the precision of flux prediction methods.

Our method demonstrated its potential to match or even surpass the accuracy of contemporary state-of-the-art approaches, such as those requiring additional flux gauges. Its main advantage lies in its capability to derive absolute flux values from pixel intensities without necessitating extra equipment, by accurately calculating the total flux of the focal spot.

The successful deployment of this method paves the way for numerous future research avenues and practical applications. For instance, it can refine the camera-target method by enabling more precise heliostat calibration through the UNet. Additionally, it can augment data-driven flux density prediction methodologies, as enhanced accuracy in flux measurements from the target leads to more precise and automated heliostat flux predictions in operational power plants. This research also underscores the potential of image-to-image neural networks in determining flux density directly from raw images. Future investigations should explore the applicability of these models in measuring combined flux densities directly at the receiver.

Overall, this work represents a step towards improving the efficiency, safety, and reliability of concentrated solar power plants. By harnessing the potential of neural networks, we can unlock new possibilities for creating data-driven predictive models that can be used to control heliostat fields and receivers, enabling the development of more efficient fully autonomous power plants.

Code availability

The code of the adapted UNet is available at: https://github.com/DLR-SF/UTIS-HeliostatBeamCharacterization

CRediT authorship contribution statement

Mathias Kuhl: Writing – review & editing, Writing – original draft, Visualization, Validation, Software, Methodology, Investigation, Formal analysis, Data curation, Conceptualization. **Max Pargmann:** Writing – review & editing, Writing – original draft, Supervision, Project administration, Funding acquisition, Formal analysis. **Mehdi Cherti:** Supervision, Methodology, Formal analysis. **Jenia Jitsev:** Writing – review & editing, Supervision, Resources, Methodology, Conceptualization. **Daniel Maldonado Quinto:** Writing – review & editing, Supervision, Project administration, Funding acquisition, Formal analysis, Conceptualization. **Robert Pitz-Paal:** Supervision, Resources, Funding acquisition.

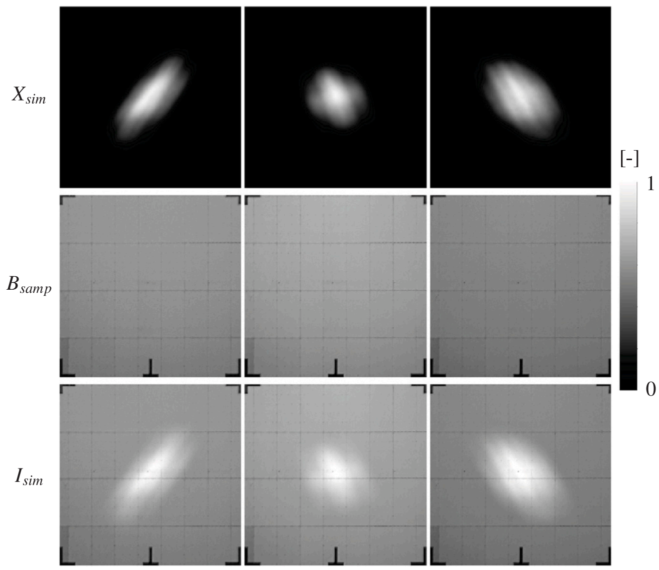

Fig. A.5. Three samples of artificially generated target images I_{sim}. The focal spots X_{sim} in the first row were simulated using a raytracer. These simulated focal spots were then combined with the sampled background images B_{samp} in the same column, according to the data generation procedure explained in Fig. 2. The resulting artificial target images I_{sim} are shown below the corresponding background images in the same column.

Declaration of competing interest

The authors declare that they have no known competing financial interests or personal relationships that could have appeared to influence the work reported in this paper.

Acknowledgments

We would like to acknowledge the funding provided by Helmholtz Association (HGF) for the *GANCSTR* project (Grant Number ZT-I-PF-5-069), within which this research was conducted.

Appendix. Data generation

See Fig. A.5.

References

[1] F. Schöniger, R. Thonig, G. Resch, J. Lilliestam, Making the sun shine at night: comparing the cost of dispatchable concentrating solar power and photovoltaics with storage, Energy Sources B Econ. Plan. Policy 16 (1) (2021) 55–74.
[2] R. Schäppi, D. Rutz, F. Dähler, A. Muroyama, P. Haueter, J. Lilliestam, A. Patt, P. Furler, A. Steinfeld, Drop-in fuels from sunlight and air, Nature 601 (7891) (2022) 63–68.
[3] L. Oberkirsch, D.M. Quinto, P. Schwarzbözl, B. Hoffschmidt, GPU-based aim point optimization for solar tower power plants, Sol. Energy 220 (2021) 1089–1098.
[4] P. González-Gómez, M.d.l.R. Rodríguez-Sánchez, M. Laporte-Azcué, D. Santana, Calculating molten-salt central-receiver lifetime under creep-fatigue damage, Sol. Energy 213 (2021) 180–197.
[5] F.J. Collado, One-point fitting of the flux density produced by a heliostat, Solar Energy 84 (4) (2010) 673–684.
[6] M.d.l.R. Rodríguez-Sánchez, C. Leray, A. Toutant, A. Ferriere, G. Olalde, Development of a new method to estimate the incident solar flux on central receivers from deteriorated heliostats, Renew. Energy 130 (2019) 182–190.
[7] R. Zhu, D. Ni, T. Yang, J. Yang, J. Chen, G. Xiao, Heliostat field aiming strategy optimization with post-installation calibration, Appl. Therm. Eng. 202 (2022) 117720.
[8] M. Pargmann, J. Ebert, D.M. Quinto, R. Pitz-Paal, S. Kesselheim, In-situ solar tower power plant optimization by differentiable ray tracing, 2023, Preprint.
[9] K.W. Stone, Automatic heliostat track alignment method, 1986, Google Patents, US Patent 4, 564, 275.
[10] S. Pomp, P. Schwarzbözl, G. Koll, F. Göhring, T. Hartz, M. Schmitz, B. Hoffschmidt, The solar tower Jülich–first operational experiences and test results, in: Proceedings, 2010.
[11] J.C. Sattler, M. Röger, P. Schwarzbözl, R. Buck, A. Macke, C. Raeder, J. Göttsche, Review of heliostat calibration and tracking control methods, Sol. Energy 207 (2020) 110–132.
[12] E. Smith, C. Ho, Field demonstration of an automated heliostat tracking correction method, Energy Procedia 49 (2014) 2201–2210.
[13] L. Guangyu, C. Zhongkun, Heliostat attitude angle detection method based on BP neural network, in: MATEC Web of Conferences, vol. 139, EDP Sciences, 2017, p. 00043.
[14] M. Pargmann, M. Leibauer, V. Nettelroth, D.M. Quinto, R. Pitz-Paal, Enhancing heliostat calibration on low data by fusing robotic rigid body kinematics with neural networks, Sol. Energy 264 (2023) 111962.
[15] P. Garcia, A. Ferriere, J.-J. Bezian, Codes for solar flux calculation dedicated to central receiver system applications: A comparative review, Sol. Energy 82 (3) (2008) 189–197.
[16] P. Schwarzbözl, R. Pitz-Paal, M. Schmitz, Visual HFLCAL-a software tool for layout and optimisation of heliostat fields, in: Proceedings, 2009.
[17] P. Leary, J. Hankins, User's Guide for MIRVAL: A Computer Code for Comparing Designs of Heliostat-Receiver Optics for Central Receiver Solar Power Plants, Technical Report, Sandia National Lab.(SNL-CA), Livermore, CA (United States), 1979.
[18] T. Wendelin, SolTRACE: a new optical modeling tool for concentrating solar optics, in: International Solar Energy Conference, Vol. 36762, 2003, pp. 253–260.
[19] J. Roccia, B. Piaud, C. Coustet, C. Caliot, E. Guillot, G. Flamant, J. Delatorre, SOLFAST, a ray-tracing Monte-Carlo software for solar concentrating facilities, in: Journal of Physics: Conference Series, vol. 369, IOP Publishing, 2012, 012029.
[20] B. Belhomme, R. Pitz-Paal, P. Schwarzbözl, S. Ulmer, A New Fast Ray Tracing Tool for High-Precision Simulation of Heliostat Fields, J. Solar Energy Eng. 131 (3) (2009) 031002.
[21] S. Ulmer, T. März, C. Prahl, W. Reinalter, B. Belhomme, Automated high resolution measurement of heliostat slope errors, Sol. Energy 85 (4) (2011) 681–687.
[22] M. Röger, C. Prahl, S. Ulmer, Fast determination of heliostat shape and orientation by edge detection and photogrammetry, in: Proc. 14th CSP SolarPACES Symposium 2008, SolarPACES, 2008.
[23] M. Röger, P. Herrmann, S. Ulmer, M. Ebert, C. Prahl, F. Göhring, Techniques to measure solar flux density distribution on large-scale receivers, J. Solar Energy Eng. 136 (3) (2014) 031013.
[24] J. Ballestrín, R. Monterreal, Hybrid heat flux measurement system for solar central receiver evaluation, Energy 29 (5–6) (2004) 915–924.
[25] J.E. Pacheco, R. Houser, A. Neumann, Concepts to Measure Flux and Temperature for External Central Receivers, Technical Report, Sandia National Labs., Albuquerque, NM (United States), 1993.
[26] H. Huang, L. Lin, R. Tong, H. Hu, Q. Zhang, Y. Iwamoto, X. Han, Y.-W. Chen, J. Wu, Unet 3+: A full-scale connected unet for medical image segmentation, in: ICASSP 2020-2020 IEEE International Conference on Acoustics, Speech and Signal Processing, ICASSP, IEEE, 2020, pp. 1055–1059.
[27] L. Liebel, M. Körner, Auxiliary tasks in multi-task learning, 2018, arXiv preprint arXiv:1805.06334.
[28] B.L. Kistler, A user's manual for DELSOL3: a computer code for calculating the optical performance and optimal system design for solar thermal central receiver plants, Technical Report, Sandia National Lab.(SNL-CA), Livermore, CA (United States), 1986.
[29] F.J. Collado, Quick evaluation of the annual heliostat field efficiency, Sol. Energy 82 (4) (2008) 379–384.